Electronic Supplementary Information (ESI)

Contents

A. Hydrogel properties

Material properties

To assess the consistency of material properties between different hydrogels, we measured the density of five white beads in three different hydration states: ambient, dry, and swollen. The "ambient" state is the condition of the beads prior to any experimentation. This state is characterized by a small amount of swelling due to ambient humidity, evidenced by slight pliability but high elastic resistance. The "dry" state was created by placing hydrogel beads in an oven at 100°C for approximately 24 hours, until the material became completely rigid. These dry beads were then placed in deionized water for 96 hours to reach their fully "swollen" state. Volumes of the spherical beads for each state were extrapolated from the diameters measured with ImageJ. The results of these experiments and calculations are displayed in Figure S1.

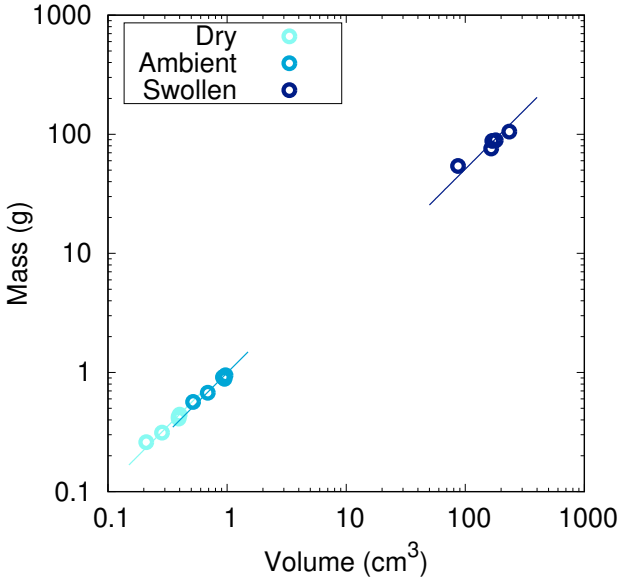

FIG. S1: Density is reasonably consistent between different hydrogels in the same state, despite scatter in their mass and volume. The three sets of points correspond to the dry, ambient, and swollen states of the hydrogel. The slope of the line for each set of points gives the average density for each set of five trials. The average densities are 1.12 g/cm^3, 0.993 g/cm^3, and 0.510 g/cm^3 for the dry, ambient, and swollen states respectively.

Size distribution

The hydrogel spheres used in the experiments have slightly different initial masses prior to swelling. This variation in size certainly impacts the location of the reported fracture threshold, as differently sized hydrogels experience different stresses in the same obstacle geometry, and limits our ability to make quantitative statements. In Fig. S2, we display the fracture data from Fig. 2 of the main text, now scaling each point by the initial mass of the hydrogel. The variation in initial mass between all trials is relatively modest, and the masses of the hydrogels in the trials close to the fracture boundary in particular are similar.

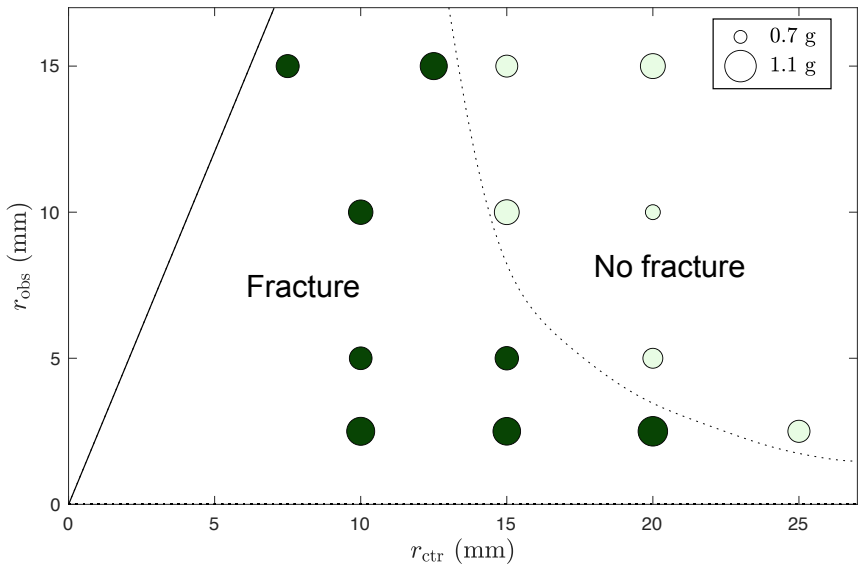

FIG. S2: Fracture threshold as a function of obstacle geometry as in Fig. 2 of the main text. The size of the points gives the initial mass of the hydrogel according to the key in the top right, with radius scaled according to mass. The dark green/light green points correspond to trials that fracture/do not fracture respectively, with the dotted line showing the approximate boundary between the two behaviors. The triangular region on the top left shows parameters for which obstacles would overlap.

B. Fracture due to vertical confinement

Hydrogel swelling in the chambers shown in Fig. 1A of the main text is limited both by the presence of obstacles as well as the top and bottom plates. In order to explore the role played by vertical confinement, we allowed hydrogels to swell in chambers with varying Δz and no obstacles.

We observed that hydrogels swelling with top and bottom plates separated by $\Delta z < 20$ mm reliably fracture even in the absence of obstacles. In contrast, for $\Delta z = 40$ mm, the separation used for all of the experiments presented in this work, we did not observe fracture in the absence of obstacles. One such trial with $\Delta z = 40$ mm is shown in Fig. S3—note that this particular hydrogel had an initial mass of 1.19 g, larger than any of the hydrogels used to create Fig. 2 of the main text.

Understanding fracture as a function of vertical confinement is an interesting direction for future research. Such a study could build on previous theoretical work on flat plate compression of a sphere [1].

C. 3D packing experiments

Following the work of Louf *et al.* [2], we allow hydrogel beads to swell in a 3D disordered granular medium composed of borosilicate glass beads of radius 1.5 mm. As described in the original work, beads of this size mimic coarse, unconsolidated soil.

We saturate the packing with deionized water and subject the entire column to an applied load of 12 pounds to prevent restructuring of the granular matrix in response to hydrogel swelling. Since the refractive index of water does

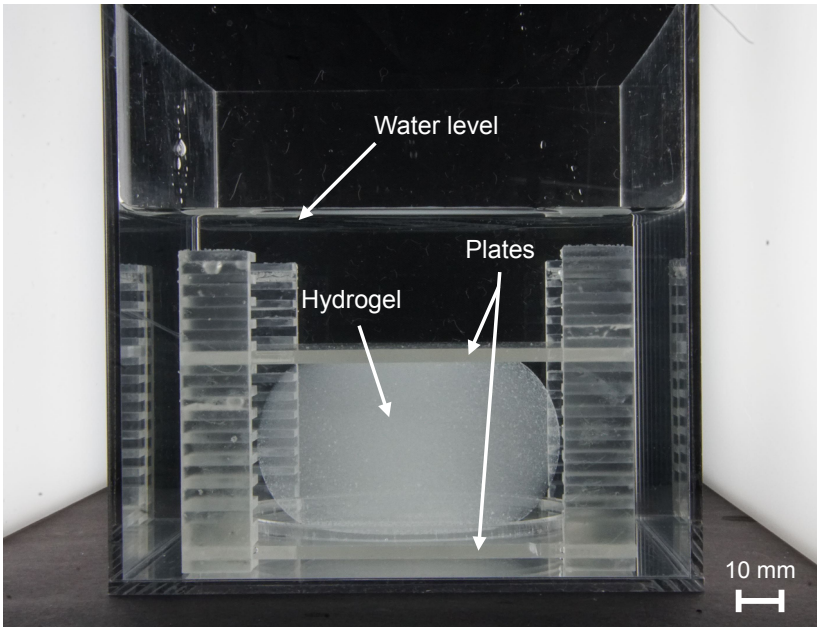

FIG. S3: A fully swollen hydrogel remains intact when compressed between two parallel plates spread 40 mm apart.

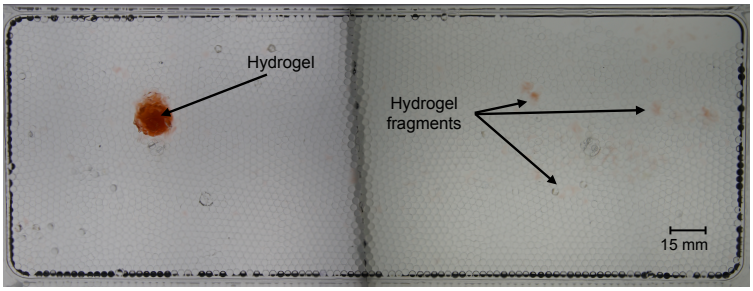

FIG. S4: Evidence of rupturing in a hydrogel swollen in a 3D granular medium. On the right side of the image, we see small orange fragments—these are pieces of the hydrogel that have broken off. The fragments are faint because they have expanded significantly relative to the main hydrogel body and are obscured by the glass beads.

not match that of the glass beads, we are unable to collect clear images of the hydrogel during swelling. However, we can disassemble the packing for visual analysis post-swelling.

After a short period of 6 hours, we see that pieces of the hydrogel have already broken off and are distributed throughout the packing (Fig. S4). When this experiment was replicated with extended swelling periods of 12, 24, and 72 hours, increasing degrees of fragmentation were observed.

Hydrogel swelling can clearly generate stresses large enough to cause rupture in 3D granular media, and hydrogel fragmentation therefore may be relevant in agriculture applications. Further studies of hydrogels exposed to water in 3D granular media are an interesting and important extension of our current work.

D. Dimensional reduction

In this section, we provide further discussion on our choice to use a 2D model and discuss the corrections we expect to have due to the 3D nature of our experiments. First, we argue that corrections due to the spherical shape of the hydrogel can be neglected near the midplane and thus locally approximate the spherical hydrogel as a cylinder. Then, we describe how an axially compressed hydrogel cylinder can be modeled in 2D via the generalized plane strain approximation.

Neglect of spherical features

To frame our discussion, we refer to Fig. S5 which shows the side view of a fully-swollen hydrogel (top view shown in Fig. 1B of the main text). From this viewpoint, we clearly see that the spherical shape preferred by the hydrogel leads to z-dependent obstacle-induced stresses—the cylindrical obstacles penetrate further into the hydrogel at the xy plane halfway between the plates compared to the xy plane at the top or bottom plate.

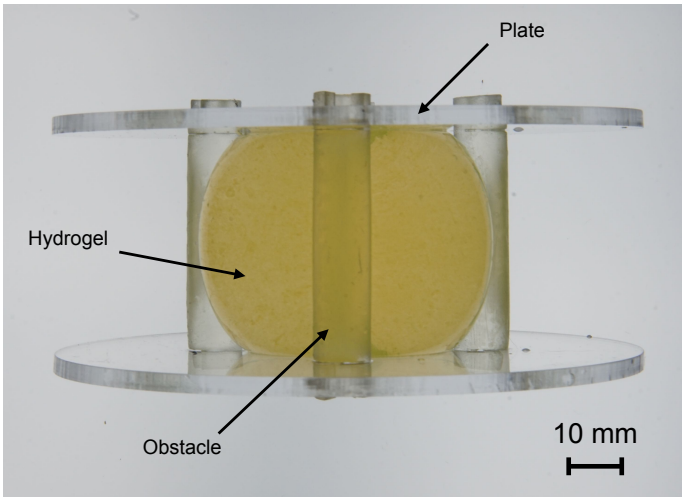

FIG. S5: Side view of the hydrogel and obstacles pictured in Fig. 1B of the main text at ~ 90 hours.

In other words, if we consider horizontal slices of the hydrogel, each slice has a preferred radius that changes as a function of z due to the spherical geometry. We can estimate this preferred radius by neglecting the shape distortion caused by the top and bottom plates (i.e., assuming the hydrogel swells to a perfect sphere in the absence of obstacles). Given a preferred sphere radius R^* and defining $z = 0$ to be halfway between the plates, the preferred disk radius r^* of a slice of the hydrogel in the xy plane as a function of z is given by

$$r^*(z) = \sqrt{R^{*2} - z^2} \approx R^* - \frac{z^2}{2R^*}. \tag{S1}$$

Indenter displacement is defined as the difference between the preferred hydrogel radius $r^*(z)$ and the leading edge of the obstacle. Since the obstacles are cylinders and their shape/location is independent of z, the z-dependent preferred hydrogel radius generates a z-dependent effective indenter displacement. For a fixed value of r_{ctr}, the dimensionless indenter displacement as a function of z is

$$\frac{\Delta(z)}{r^*(z)} = \frac{r^*(z) - r_{\text{ctr}}}{r^*(z)} \approx \left(1 - \frac{r_{\text{ctr}}}{R^*}\right) - \frac{r_{\text{ctr}}}{2R^*}\left(\frac{z^2}{R^{*2}}\right). \tag{S2}$$

When corrections of order z^2/R^{*2} can be neglected, we can ignore the z-dependence and locally approximate the hydrogel as a cylinder. This approximation is reasonable close to the midplane of the hydrogel, where the confinement is greatest.

Thus, we assume our system meets the criteria of a generalized plane strain approximation near the midplane of the hydrogel at equilibrium. We next describe this approximation, first in the context of linear elasticity and then in the context of the nonlinear hydrogel model. We emphasize that this dimensional reduction only holds in equilibrium, as the dynamic features observed in experiments, including initial swelling as well as fracture itself, have 3D features that cannot be straightforwardly described in 2D.

Generalized plane strain: Hookean elasticity

Generalized plane strain approximations can describe a cylinder in frictionless contact with walls that impose a uniform axial contraction, experiencing tractions independent of z on its sides [3]. Accordingly, we assume that the strain tensor elements u_{xx}, u_{xy} and u_{yy} are independent of z, $u_{xz} = u_{yz} = 0$, and $u_{zz} = \alpha$, a constant. Assuming

Hooke's law holds, we can write down the standard equations for the stress tensor σ_{ij} in terms of the strain tensor u_{ij}, bulk Young's modulus E_{3D}, and bulk Poisson's ratio ν_{3D} [4].

$$\sigma_{xx} = \frac{E_{3D}}{(1+\nu_{3D})(1-2\nu_{3D})}\left((1-\nu_{3D})u_{xx} + \nu_{3D}\left(u_{yy}+\alpha\right)\right), \tag{S3}$$

$$\sigma_{xy} = \frac{E_{3D}}{1+\nu_{3D}}u_{xy}, \tag{S4}$$

$$\sigma_{yy} = \frac{E_{3D}}{(1+\nu_{3D})(1-2\nu_{3D})}\left((1-\nu_{3D})u_{yy} + \nu_{3D}\left(u_{xx}+\alpha\right)\right), \tag{S5}$$

$$\sigma_{xz} = \sigma_{yz} = 0, \tag{S6}$$

$$\sigma_{zz} = \frac{E_{3D}}{(1+\nu_{3D})(1-2\nu_{3D})}\left((1-\nu_{3D})\alpha + \nu_{3D}\left(u_{xx}+u_{yy}\right)\right), \tag{S7}$$

Since $\frac{\partial \sigma_{zz}}{\partial z} = \sigma_{xz} = \sigma_{yz} = 0$, there are only two equations of equilibrium. Note that α drops out of the equilibrium equations entirely.

To make comparisons with 2D elasticity, it will also be useful to express the strains in terms of stresses. In order to do this, we write σ_{zz} in terms of σ_{xx} and σ_{yy} using the relation for u_{zz}.

$$\sigma_{zz} = \nu_{3D}(\sigma_{xx}+\sigma_{yy}) + E_{3D}\alpha. \tag{S8}$$

Using this relation, the elements of the strain tensor are

$$u_{xx} = \frac{1-\nu_{3D}^2}{E_{3D}}\sigma_{xx} - \frac{\nu_{3D}(1+\nu_{3D})}{E_{3D}}\sigma_{yy} - \nu_{3D}\alpha, \tag{S9}$$

$$u_{xy} = \frac{(1+\nu_{3D})}{E_{3D}}\sigma_{xy}, \tag{S10}$$

$$u_{yy} = \frac{1-\nu_{3D}^2}{E_{3D}}\sigma_{yy} - \frac{\nu_{B}(1+\nu_{3D})}{E_{3D}}\sigma_{xx} - \nu_{3D}\alpha, \tag{S11}$$

$$u_{zz} = \alpha, \qquad u_{yz} = u_{xz} = 0. \tag{S12}$$

When $\alpha = 0$, we recover the standard plane strain result.

Relation to 2D elastic solid

We compare the stress and strain tensors derived using the generalized plane strain approximation to those of a 2D elastic solid. For a 2D material, there is no z direction. The two equilibrium equations are therefore identical to those for generalized plane strain. However, the relationship between stress and strain differs. Strain tensor elements are given in terms of stress tensor elements as

$$u_{xx} = \frac{1}{E_{2D}}\sigma_{xx} - \frac{\nu_{2D}}{E_{2D}}\sigma_{yy}, \tag{S13}$$

$$u_{xy} = \frac{(1+\nu_{2D})}{E_{2D}}\sigma_{xy}, \tag{S14}$$

$$u_{yy} = \frac{1}{E_{2D}}\sigma_{yy} - \frac{\nu_{2D}}{E_{2D}}\sigma_{xx}, \tag{S15}$$

where $E_{2D} = \frac{4\mu(\mu+\lambda)}{2\mu+\lambda}$ and $\nu_{2D} = \frac{\lambda}{2\mu+\lambda}$ are the 2D Young's modulus and Poisson's ratio defined in terms of 2D Lamé parameters μ and λ. We observe that if we make the substitutions $E_{2D} \to \frac{E_{3D}}{1-\nu_{3D}^2}$ and $\nu_{2D} \to \frac{\nu_{3D}}{1-\nu_{3D}}$ and subtract $\nu_{3D}\alpha\delta_{ij}$, we can transform the 2D strain tensor into the generalized plane strain tensor.

Therefore, if we solve for the stresses using a 2D model, we can create solutions to a corresponding generalized plane strain model using the procedure described above.

Generalized plane strain: nonlinear hydrogel theory

Thus far, we have only discussed the generalized plane strain approximation in the context of Hookean elasticity. We show here how the same kinematic assumptions affect the nonlinear hydrogel model when deformations are not necessarily small.

The free energy density of a 3D hydrogel is [5, 6]:

$$\frac{F_{\text{en}}}{V_0 k_B T} = \frac{n_p^{3D}}{2}\left(F_{iK}^{3D}F_{iK}^{3D} - 3 - 2\ln(\det(\mathbf{F}^{3D}))\right) + \frac{1}{v}\left(vC_{3D}\ln\left(\frac{vC_{3D}}{1+vC_{3D}}\right) + \chi\frac{vC_{3D}}{1+vC_{3D}}\right), \tag{S16}$$

where $\mathbf{F}^{3D}$ is the 3D deformation gradient tensor, v is the volume of a solvent molecule, n_p^{3D} is the number of polymer chains per unit reference volume V_0, and C_{3D} is the 3D nominal concentration (number of solvent molecules per unit reference volume).

The Cauchy stress is given by

$$\sigma_{ij} = \frac{n_p^{3D}k_BT}{J_{3D}}\left(F_{iK}^{3D}F_{jK}^{3D} - \delta_{ij}\right) + \frac{k_BT}{vJ_{3D}}\mathcal{A}(J_{3D})\delta_{ij} - \frac{\mu_{3D}}{v}\delta_{ij}, \tag{S17}$$

where we define the function

$$\mathcal{A}(J_{3D}) \equiv \left(J_{3D}\ln\left(\frac{J_{3D}-1}{J_{3D}}\right) + 1 + \frac{\chi}{J_{3D}}\right). \tag{S18}$$

We now apply our generalized plane strain assumptions. The deformation gradient tensor and its inverse can be written

$$\mathbf{F}^{3D} = \begin{pmatrix} F_{xX} & F_{xY} & 0 \\ F_{yX} & F_{yY} & 0 \\ 0 & 0 & \lambda_z \end{pmatrix}, \qquad (\mathbf{F}^{3D})^{-1} = \begin{pmatrix} F_{yY}/J & -F_{xY}/J & 0 \\ -F_{yX}/J & F_{xX}/J & 0 \\ 0 & 0 & 1/\lambda_z \end{pmatrix}, \tag{S19}$$

where J is the determinant of the 2D deformation gradient tensor F_{iK} and $\lambda_z = 1+\alpha$ is the axial stretch. Thus, $J_{3D} = \lambda_z J$. Constrained hydrogel swelling is well-studied—Ref. [7] provides a particularly relevant analysis of indentation on swollen constrained hydrogels.

With these assumptions, $\sigma_{xz} = \sigma_{yz} = 0$, and σ_{zz} is given by

$$\sigma_{zz} = \frac{k_BT}{v}\left(\frac{n_p^{3D}v}{\lambda_z J}\left(\lambda_z^2 - 1\right) + \frac{\mathcal{A}(\lambda_z J)}{\lambda_z J} - \frac{\mu_{3D}}{k_BT}\right). \tag{S20}$$

As in Hookean elasticity, this stress is independent of z and fully determined by the strains in the x and y directions and the prescribed stretch in the z direction. Therefore, $\frac{\partial \sigma_{zz}}{\partial z} = 0$ and there are again only two equilibrium equations to solve. In the absence of body forces, these are $\frac{\partial \sigma_{xj}}{\partial x_j} = 0$ and $\frac{\partial \sigma_{yj}}{\partial x_j} = 0$.

The other nonzero elements of the Cauchy stress tensor can be written

$$\frac{\sigma_{ij}}{k_BT} = \frac{n_p^{3D}F_{iK}F_{jK}}{\lambda_z J} + \frac{1}{v}\left(\frac{\mathcal{A}(\lambda_z J)}{\lambda_z J} - \frac{n_p^{3D}v}{\lambda_z J} - \frac{\mu_{3D}}{k_BT}\right)\delta_{ij}. \tag{S21}$$

In the absence of obstacles, the hydrogel will swell isotropically in x and y, reaching an equilibrium swelling stretch ratio λ_0 that will be a function of λ_z.

We find λ_0 by setting $\sigma_{ij} = 0$ with $F_{iJ} = \lambda_0\delta_{iJ}$, $J = \lambda_0^2$. This gives the relation

$$\frac{\mu_{3D}}{k_BT} = \frac{n_p^{3D}v}{\lambda_z}\left(1 - \frac{1}{\lambda_0^2}\right) + \frac{1}{\lambda_z\lambda_0^2} + \ln\left(1 - \frac{1}{\lambda_z\lambda_0^2}\right) + \frac{\chi}{\lambda_z^2\lambda_0^4}. \tag{S22}$$

This equation must be solved numerically. The relationship between λ_z and λ_0 for $\mu_{3D} = 0$, $n_p^{3D}v = 0.001$, $\chi = 0.3$ is shown in Fig. S6. When $\lambda_z = \lambda_0$, we regain the standard 3D result [8].

Relation to 2D hydrogel

We compare the stress tensor for a hydrogel in generalized plane strain to that of the purely 2D hydrogel described in the main text. For the energy functional

$$\frac{F_{\text{en}}}{A_0 k_BT} = \frac{n_p}{2}\left(F_{iK}F_{iK} - 2 - 2\ln(\det(\mathbf{F}))\right) + \frac{1}{\Omega}\left(\Omega C\ln\left(\frac{\Omega C}{1+\Omega C}\right) + \chi\frac{\Omega C}{1+\Omega C}\right). \tag{S23}$$

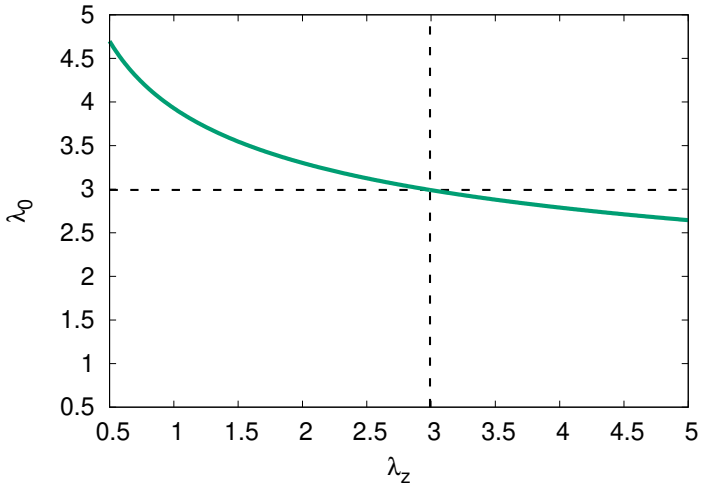

FIG. S6: Isotropic transverse stretch λ_0 as a function of imposed axial stretch λ_z for $\mu_{3D} = 0, n_p^{3D} v = 0.001, \chi = 0.3$. The dashed lines show $\lambda_z = \lambda_0$, which corresponds to free swelling in 3D.

The corresponding Cauchy stresses are

$$\frac{\sigma_{ij}}{k_B T} = \frac{n_p F_{iK} F_{jK}}{J} + \frac{1}{\Omega}\left(\frac{\mathcal{A}(J)}{J} - \frac{n_p \Omega}{J} - \frac{\mu}{k_B T}\right)\delta_{ij}, \tag{S24}$$

where

$$\mathcal{A}(J) = \left(J \ln\left(\frac{J-1}{J}\right) + 1 + \frac{\chi}{J}\right). \tag{S25}$$

We can use 2D solutions to construct generalized plane strain solutions with arbitrary λ_z. If we make the following substitutions in Eq. (S24), we regain Eq. (S21).

$$F_{iJ} \to \sqrt{\lambda_z} F_{iJ}, \tag{S26}$$
$$J \to \lambda_z J, \tag{S27}$$
$$n_p \to \frac{n_p^{3D}}{\lambda_z}, \tag{S28}$$
$$\Omega \to v, \tag{S29}$$
$$\frac{\mu}{k_B T} \to \frac{\mu_{3D}}{k_B T} - \frac{n_p^{3D} v}{\lambda_z J}\left(\frac{1}{\lambda_z} - 1\right). \tag{S30}$$

Note that, as in the Hookean elasticity example, these substitutions change the units of various terms—this occurs because 2D and 3D stress have different units.

Summary

Our experimental system can be reasonably modeled in 2D using generalized plane strain assumptions near the hydrogel midsection in equilibrium. In the main text, we work with 2D elastic models to simplify our calculations and simulations. As described above, it is straightforward to transform 2D elasticity solutions to generalized plane strain solutions and vice versa. The imposed stretch in the z direction enters as an effective chemical potential in the hydrogel model, so chemical potential boundary conditions in the 2D simulations would need to be modified to make more quantitative comparisons with experiments.

E. Dynamics

We simulate hydrogel swelling dynamically using the kinetic law proposed in Hong *et al.* [5].

$$j_i = -\frac{cD}{k_B T}\frac{\partial \mu}{\partial x_i}, \tag{S31}$$

where j_i and c are the solvent flux and concentration in the current configuration respectively, μ is the chemical potential, and D is solvent diffusivity. To evolve the concentration field, we discretize the continuity equation using the concentration and solvent flux in the reference configuration: $\frac{\partial C}{\partial t} + \frac{\partial J_K}{\partial X_K} = 0$, with $J_K = \det(\mathbf{F})\frac{\partial X_K}{\partial x_i} j_i$ [9].

We do not expect the dynamical behavior of our simulations to closely reproduce what we observe in our experiments for several reasons. First, the kinetic law we use is simple and does not account for effects such as changes to the diffusion constant as the polymer network expands. See, e.g., [10–12], for further discussions about appropriate expressions for solvent flux. Second, before the hydrogel makes contact with the top and bottom plates, it swells equally in all three dimensions. A 2D simulation therefore only provides a reasonable approximation of equilibrium experimental behavior, as discussed in ESI Sec. D.

Nevertheless, the simulated 2D dynamics are interesting and complex, and are relevant to hydrogel geometries that remain quasi-2D throughout the swelling process, such as a thin hydrogel disk between two flat plates. We therefore show some characteristic results and provide a brief discussion on simulated dynamical behavior here. In all cases, we initialize the model at a radius r_0 and impose an isotropic initial stretch $\lambda_x = \lambda_y = 1.5$ to avoid the singularity that appears for the dry state with $\lambda_x = \lambda_y = 1$ [8]. As described in *Materials and methods*, simulations are run until they reach equilibrium which occurs at different times for different trials.

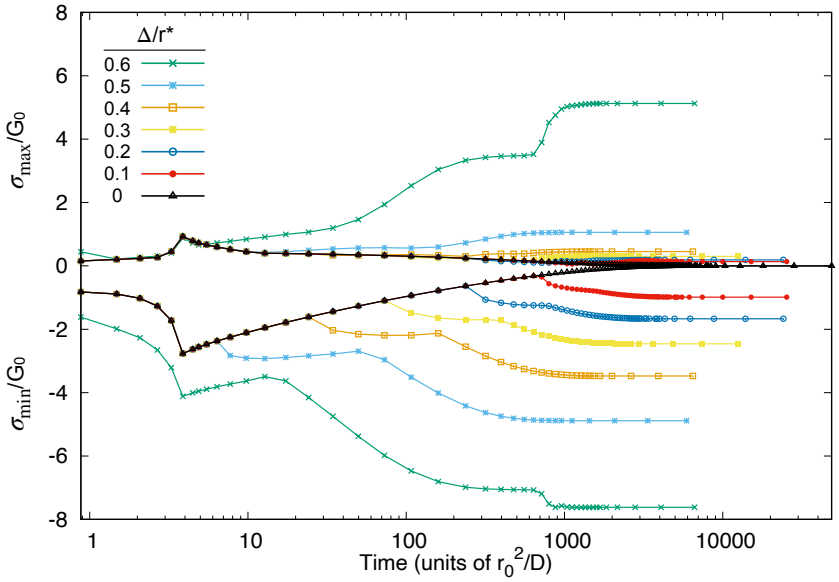

FIG. S7: Maximum tensile and compressive principal stresses as a function of time (rescaled by r_0, the dry hydrogel radius, and D, the diffusivity) for $r_{\text{obs}}/r^* = 0.3$, varying Δ/r^*.

In Fig. S7, we show the maximum principal tensile (top set of curves) and compressive (bottom set of curves) stresses as a function of time for different values of Δ/r^* with $r_{\text{obs}}/r^* = 0.3$. These data are a subset of the data displayed in Fig. 5 of the main text, with maxima/minima taken over the entire mesh.

To understand these data, we use the $\Delta/r^* = 0$ curve as a reference. This curve corresponds to the unconstrained case. We observe a peak in both the maximum compressive and tensile principal stresses at dimensionless time $\hat{t} \equiv \frac{tD}{r_0^2} \approx 4$, followed by a decay to zero. This peak in stress occurs because the outer regions of the hydrogel swell faster than the inner regions, and can lead to the formation of transient cusp structures, as described in the main text and elsewhere [13]. For $\Delta/r^* \leq 0.5$, simulations follow the free swelling curve until they make contact with the obstacles. Following contact, the hydrogel develops stresses that do not disappear at equilibrium. The data for $\Delta/r^* = 0.6$, the strongest confinement shown here, has a number of interesting differences from the other trials. This hydrogel encounters obstacles prior to the time points shown in Fig. S7, and thus sustains larger stresses earlier compared to the other trials. At $\hat{t} \approx 700$, we see a sharp increase in both the compressive and tensile stresses in this trial, not observed in other trials—this is the symmetry-breaking instability discussed in Sec. IIID of the main text.

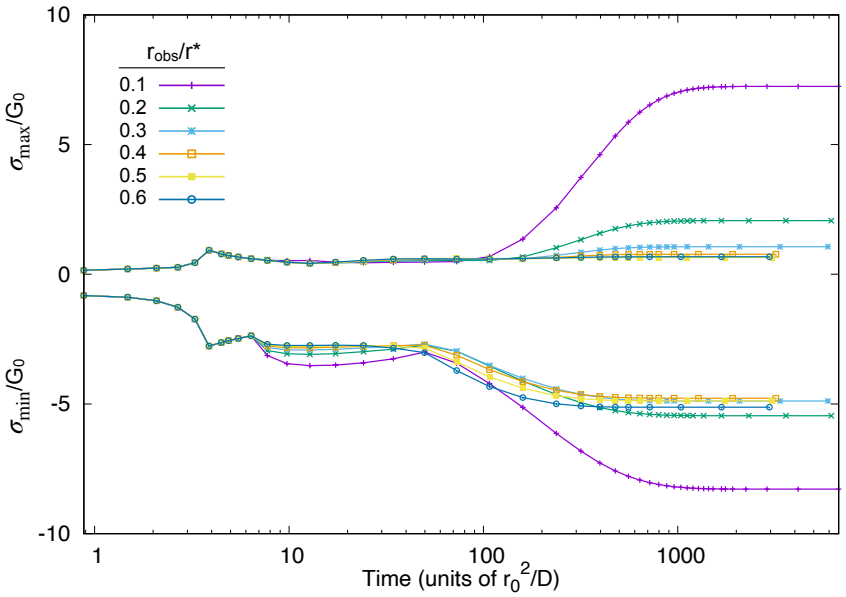

FIG. S8: Maximum tensile and compressive principal stresses as a function of time (rescaled by r_0, the dry hydrogel radius, and D, the diffusivity) for $\Delta/r^* = 0.5$, varying $r_{\rm obs}/r^*$. The light blue curves in this figure and Fig. S7 display the same data.

We compare these dynamics to those in Fig. S8. Here, we show principal stresses as a function of time with Δ/r^* held fixed and $r_{\rm obs}/r^*$ varied, again with maxima/minima taken over the entire mesh. These data correspond to vertical slices of Figs. 5(A,B). Since Δ/r^* is the same for all trials, the hydrogels all encounter obstacles at the same time, $\hat{t} \approx 6$. After that time, trials behave differently due to the different curvature of the obstacles.

F. Elastic moduli

In this section, we provide the derivation for the effective Poisson's ratio and Young's modulus of a 2D hydrogel in equilibrium (Eqs. (2) and (3) of the main text) by adapting the argument presented in Bouklas and Huang [14]. We begin with the Cauchy stress for a 2D hydrogel model,

$$\frac{\Omega\sigma_{ij}}{k_BT} = \frac{n_p\Omega}{J}F_{iK}F_{jK} + \left(\frac{\mathcal{A}(J)}{J} - \frac{n_p\Omega}{J} - \frac{\mu}{k_BT}\right)\delta_{ij}, \tag{S32}$$

with

$$\mathcal{A}(J) = \left(J\ln\left(\frac{J-1}{J}\right) + 1 + \frac{\chi}{J}\right). \tag{S33}$$

We apply a uniaxial stress in the x direction and require $\sigma_{yy} = 0$. This sets

$$0 = \frac{\Omega\sigma_{yy}}{k_BT} = \frac{n_p\Omega}{\lambda_x\lambda_y}\left(\lambda_y^2 - 1\right) + \left(\frac{\mathcal{A}(\lambda_x\lambda_y)}{\lambda_x\lambda_y} - \frac{\mu}{k_BT}\right). \tag{S34}$$

We assume that the resulting stretches are small deformations relative to the stress-free equilibrium state with stretch λ_0, defined for the 2D hydrogel via the equation

$$\frac{\mu}{k_BT} = \frac{n_p\Omega}{\lambda_0^2}\left(\lambda_0^2 - 1\right) + \frac{\mathcal{A}(\lambda_0^2)}{\lambda_0^2} = n_p\Omega\left(1 - \frac{1}{\lambda_0^2}\right) + \ln\left(1 - \frac{1}{\lambda_0^2}\right) + \frac{1}{\lambda_0^2} + \frac{\chi}{\lambda_0^4}. \tag{S35}$$

This allows us to define the strain tensor elements in terms of stretches as

$$\lambda_x = \lambda_0(1 + u_{xx}), \tag{S36}$$
$$\lambda_y = \lambda_0(1 + u_{yy}). \tag{S37}$$

We next expand Eq. (S34) to linear order in u_{xx} and u_{yy}.After simplifying using Eq. (S35), our result is

$$u_{xx}\left(n_p\Omega\left(1-\frac{1}{\lambda_0^2}\right)+\frac{2\chi}{\lambda_0^4}-\frac{1}{\lambda_0^2(\lambda_0^2-1)}\right)=u_{yy}\left(n_p\Omega\left(1+\frac{1}{\lambda_0^2}\right)+\frac{1}{\lambda_0^2(\lambda_0^2-1)}-\frac{2\chi}{\lambda_0^4}\right). \tag{S38}$$

Defining the Poisson's ratio as

$$\nu=-\frac{u_{yy}}{u_{xx}}, \tag{S39}$$

we find

$$\nu=\frac{n_p\Omega\left(\frac{1}{\lambda_0^2}-1\right)+\frac{1}{\lambda_0^2(\lambda_0^2-1)}-\frac{2\chi}{\lambda_0^4}}{n_p\Omega\left(\frac{1}{\lambda_0^2}+1\right)+\frac{1}{\lambda_0^2(\lambda_0^2-1)}-\frac{2\chi}{\lambda_0^4}}=1-\frac{2n_p\Omega}{n_p\Omega\left(1+\frac{1}{\lambda_0^2}\right)+\frac{1}{\lambda_0^2(\lambda_0^2-1)}-\frac{2\chi}{\lambda_0^4}}. \tag{S40}$$

To find the Young's modulus, we perform the same operations in the equation for σ_{xx}:

$$\frac{\Omega\sigma_{xx}}{k_BT}=\frac{n_p\Omega}{\lambda_x\lambda_y}\left(\lambda_x^2-1\right)+\left(\frac{\mathcal{A}(\lambda_x\lambda_y)}{\lambda_x\lambda_y}-\frac{\mu}{k_BT}\right). \tag{S41}$$

We substitute $u_{yy}=-\nu u_{xx}$ and expand in u_{xx} to linear order. After simplifying, we find

$$\frac{\Omega\sigma_{xx}}{k_BT}=2(1+\nu)n_p\Omega u_{xx}. \tag{S42}$$

Thus, the effective 2D Young's modulus is

$$E=2(1+\nu)n_pk_BT, \tag{S43}$$

and the effective 2D shear modulus is

$$G_0\equiv\frac{E}{2(1+\nu)}=n_pk_BT. \tag{S44}$$

Robustness of mapping

In the derivation of effective elastic parameters, we neglect terms quadratic in u_{ij}. Thus, for large deformations, we expect our mapping between hydrogel model parameters and linear elastic parameters [Eqs. (S40) and (S44)] to become inaccurate (i.e., the effective Poisson's ratio and Young's modulus will acquire a dependence on strain). This additional source of nonlinearity has the potential to complicate our comparisons between the nonlinear hydrogel model and the St. Venant-Kirchhoff model in Sec. IIIB and C of the main text. For example, an inhomogeneous strain state could induce spatially-varying effective elastic parameters. However, using simulations of a neo-Hookean elastic model, we argue that this nonlinearity can be neglected for the deformations considered in this work.

We simulate a compressible neo-Hookean elastic model in FEniCS, using the same mesh resolution as in the hydrogel trials (approximately 30 vertices across the radius; see Fig. 3, left column). The strain-energy density function is

$$W=\frac{G_0}{2}\left(F_{iK}F_{iK}-2-2\ln(\det(\mathbf{F}))\right)+\frac{G_0\nu}{1-\nu}\ln(\det(\mathbf{F}))^2, \tag{S45}$$

where the 2D shear modulus G_0 and Poisson's ratio ν are set according to Eqs. (S40) and (S44). Setting the coefficients in this manner ensures consistency with linear elasticity. Displacements are defined relative to the zero stress reference configuration with radius r^*.

In Fig. S9, we compare the maximum principal stresses in the neo-Hookean elastic model and the hydrogel model. Although there are some differences between the two data sets, it is difficult to tell whether these differences increase as a function of strain as expected. We learn more by comparing the stress profiles directly in Fig. S10. As Δ/r^* increases, we clearly see differences between the models increase. However, deviations only appear at the largest values of Δ/r^* tested, and even then, they remain small relative to the magnitude of the stress. These comparisons suggest that our mapping from hydrogel parameters to elastic parameters is reasonably accurate, perhaps even surprisingly so, for large indentation-type deformations.

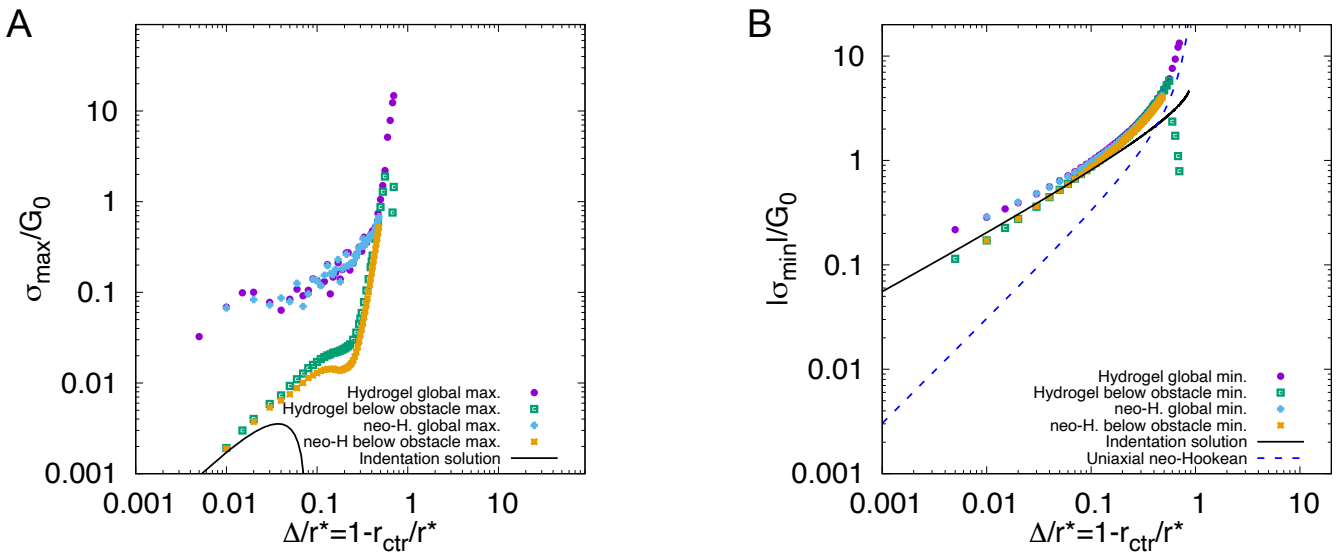

FIG. S9: Comparison between maximum principal Cauchy tensile and compressive stresses in simulations with the nonlinear hydrogel model and neo-Hookean elastic model. Results for the neo-Hookean model are shown through $\Delta/r^* = 0.48$. Even for these large deformations, we observe reasonably good agreement between the two models. Note that we plot both the maximum/minimum principal stress over the entire hydrogel domain (labeled global max./min.) as well as the maximum/minimum principal stress along the line connecting the hydrogel center to an obstacle center (labeled below obstacle max./min.). For further discussion of the differences between these two measures, see ESI Sec. I. In panel B, the dashed line shows Eq. 10 of the main text for comparison.

G. Indentation solutions

Here we derive the indentation theory equations in Sec. IIIA of the main text. We start with the Flamant solution applied to a point force ζ acting normal to an elastic half space in 2D [15]. We assume the half space fills the region $y < 0$ and use the convention that $\zeta < 0$ corresponds to a force that compresses the plane. In radial coordinates with the origin at the location at which the point force acts, this is a simple radial stress distribution

$$\sigma_{rr} = -\frac{\zeta \sin\theta}{\pi r}. \tag{S46}$$

Directly beneath the point source, $\theta = -\pi/2$ and $\sigma_{rr} = \frac{\zeta}{\pi r} < 0$.

The displacements due to a point force grow logarithmically in 2D. Therefore, we must be mindful of boundaries, as the finite size of our deformable material will influence our calculations. We can gain an appreciation for this subtlety by considering two diametrically opposed point forces acting on the top and bottom of a 2D elastic disk, as in Goodier and Timoshenko [16] p 107. In this case, all points on the boundary of the disk experience isotropic compression due to the pair of point forces, and a uniform tension $\sigma_{ij} = -\frac{\zeta}{\pi r^*}\delta_{ij}$ must be added to maintain a stress-free boundary. By the same argument, $\sigma_{ij} = -\frac{2\zeta}{\pi r^*}\delta_{ij}$ must be added to the stress tensor to free the boundaries when four perpendicular point forces are acting on the elastic disk.

We now consider the specific geometry we are interested in: four circular indenters of radius r_{obs} acting on an elastic disk of radius r^*. In the weak confinement regime, we expect the greatest stresses to develop on the line connecting the center of the elastic disk and the center of an indenter, as stresses go to zero at the points at which the disk and indenter lose contact. Therefore, by symmetry we only need to solve for stresses along this line ($x = 0$ line in inset to Fig. 4B in the main text). Appealing to Saint-Venant's principle, we simplify our calculation by modeling one obstacle as a 2D Hertzian indenter and the other three obstacles as point forces. We proceed by generalizing the calculation in Johnson [17] p129.

We place the origin at the center of the contact between the elastic body and the Hertzian indenter, and let $b > 0$ be the distance from this origin along the centerline with $x = 0$. The stress tensor contributions from the point indenters

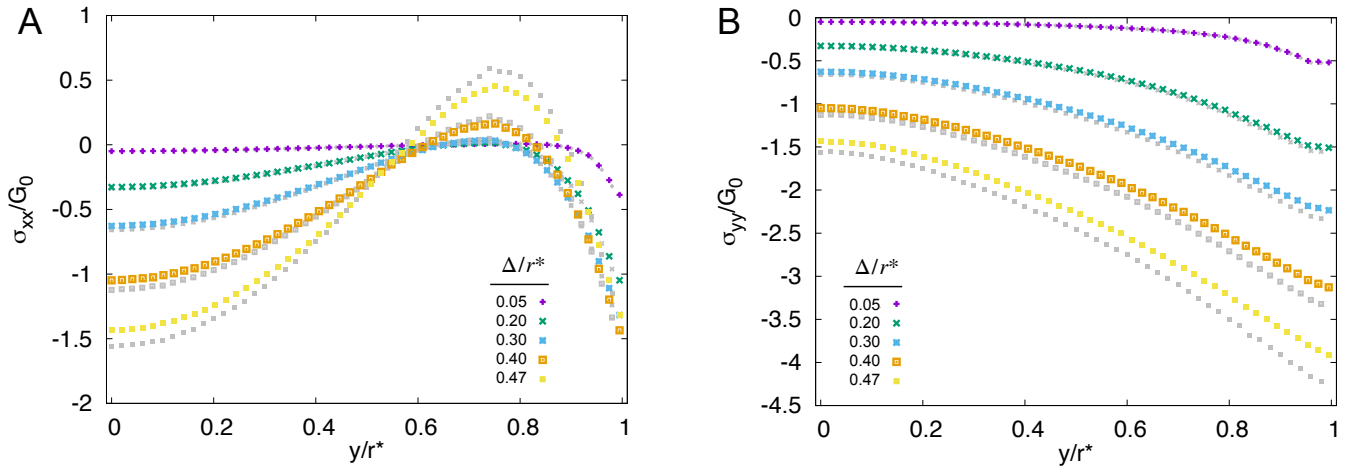

FIG. S10: Comparison between Cauchy stress profiles in simulations with the nonlinear hydrogel model and neo-Hookean elastic model, plotted against undeformed fully-swollen coordinates (corresponding to an unobstructed equilibrium state for the hydrogel). Neo-Hookean results are shown with large colored markers, while hydrogel results are shown in grey. Data corresponding to the same value of Δ/r^* have the same marker shape. Although we clearly see differences between the two models at large Δ/r^*, the two models produce similar stress profiles.

along the line of interest are

$$\sigma_{xx} = \frac{4\zeta r^{*3}}{\pi(r^{*2} + (r^* - b)^2)^2}, \tag{S47}$$

$$\sigma_{yy} = \frac{2\zeta}{\pi(2r^* - b)} + \frac{4\zeta r^*(r^* - b)^2}{\pi(r^{*2} + (r^* - b)^2)^2}, \tag{S48}$$

$$\sigma_{xy} = 0. \tag{S49}$$

The Hertzian indenter contributes

$$\sigma_{xx} = \frac{\zeta}{\pi}\left(\frac{2(a^2 + 2b^2)}{a^2\sqrt{a^2 + b^2}} - \frac{4b}{a^2}\right), \tag{S50}$$

$$\sigma_{yy} = \frac{2\zeta}{\pi\sqrt{a^2 + b^2}}, \tag{S51}$$

$$\sigma_{xy} = 0, \tag{S52}$$

where the contact length $2a$ is given according to

$$a^2 = -\frac{4\zeta}{E\pi}\left(\frac{1}{r_{\text{obs}}} + \frac{1}{r^*}\right)^{-1}. \tag{S53}$$

The stress tensor is the sum of these contributions, plus the isotropic tension from the corrective solution, $\sigma_{ij} = -\frac{2\zeta}{\pi r^*}\delta_{ij}$. With the substitution $y = r^* - b$, we find Eqs. (4)-(7) of the main text.

The strain u_{yy} can be found as

$$u_{yy} = \frac{\sigma_{yy}}{E} - \frac{\nu}{E}\sigma_{xx}. \tag{S54}$$

We find the displacement at the surface directly beneath the indenter by integrating

$$-\Delta = \int_0^{r^*} u_{yy}(b)db. \tag{S55}$$

We expand this expression in the limit $a/r^* \ll 1$, neglecting terms quadratic in a/r^* to find

$$\Delta = -\frac{\zeta}{E\pi}\left(\ln\left(\frac{16r^{*2}}{a^2}\right) + \frac{1}{2}(\pi - 6 - \pi\nu)\right). \tag{S56}$$

This expression can be inverted using the Lambert W-function or product logarithm ([18], §4.13). Note that this function is multivalued for small indenter force and the $k = -1$ branch must be chosen for consistent results.

H. St. Venant-Kirchhoff model

As described in Sec. IIIB of the main text, we simulate St. Venant-Kirchhoff materials surrounded by four circular indenters in FEniCS. We use the same mesh as in the hydrogel trials (approximately 30 vertices across the radius; see Fig. 3, left column). The strain-energy density function is

$$W = G_0 u_{ij}^2 + \frac{\lambda}{2}u_{kk}^2 = G_0\left(u_{ij}^2 + \frac{\nu}{1-\nu}u_{kk}^2\right), \tag{S57}$$

$$u_{ij} = \frac{1}{2}\left(\frac{\partial u_i}{\partial x_j} + \frac{\partial u_j}{\partial x_i} + \frac{\partial u_k}{\partial x_i}\frac{\partial u_k}{\partial x_j}\right), \tag{S58}$$

where $G_0 = \frac{Y}{2(1+\nu)}$ and $\lambda = \frac{Y\nu}{1-\nu^2} = \frac{2G_0\nu}{1-\nu}$ are Lamé coefficients, set to match the effective elastic properties of the hydrogel as described in ESI Sec. F, u_i is a displacement in the ith direction, and indices run over x and y. Displacements are defined relative to the zero stress reference configuration with radius r^*.

As the indenter displacement increases, St. Venant-Kirchhoff simulations can become unstable. For example, due to the linear constitutive law, there is a finite energetic cost for compressing material to a point [19]. To maintain stability when possible, we incrementally increase both indenter displacement and penalty strength. Nonetheless, we cannot simulate values of $\Delta/r^* > 0.115$ for $r_{\text{obs}}/r^* = 0.3$. Results from these simulations prior to this threshold are shown in Fig. S11 and S12.

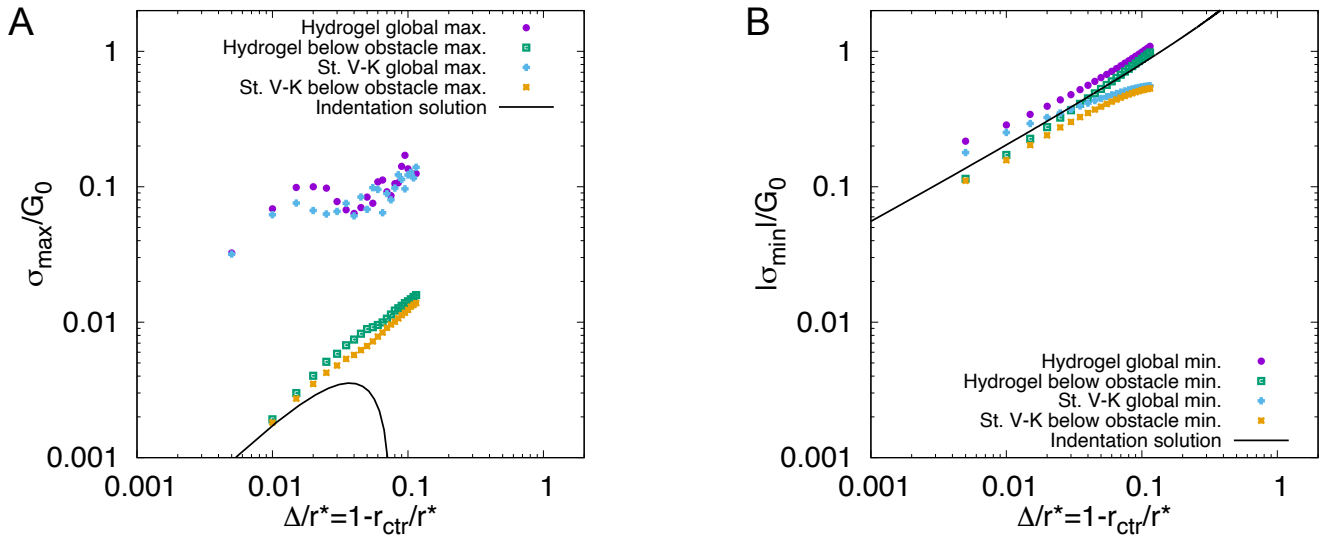

FIG. S11: Comparison between maximum principal Cauchy tensile and compressive stresses in simulations with the nonlinear hydrogel model and St. Venant-Kirchhoff model. In (A), we observe that the St. Venant-Kirchhoff model produces approximately the same tensile stresses as the hydrogel model, implying that a geometric nonlinearity can explain tensile stresses up to $\sim \Delta/r^* = 0.115$. In (B), we see that the St. Venant-Kirchhoff model displays compressive stresses that are lower than the hydrogel model, implying that a material nonlinearity is responsible for the additional compressive stress. Note that we plot both the maximum/minimum principal stress over the entire hydrogel domain (labeled global max./min.) as well as the maximum/minimum principal stress along the line connecting the hydrogel center to an obstacle center (labeled below obstacle max./min.).

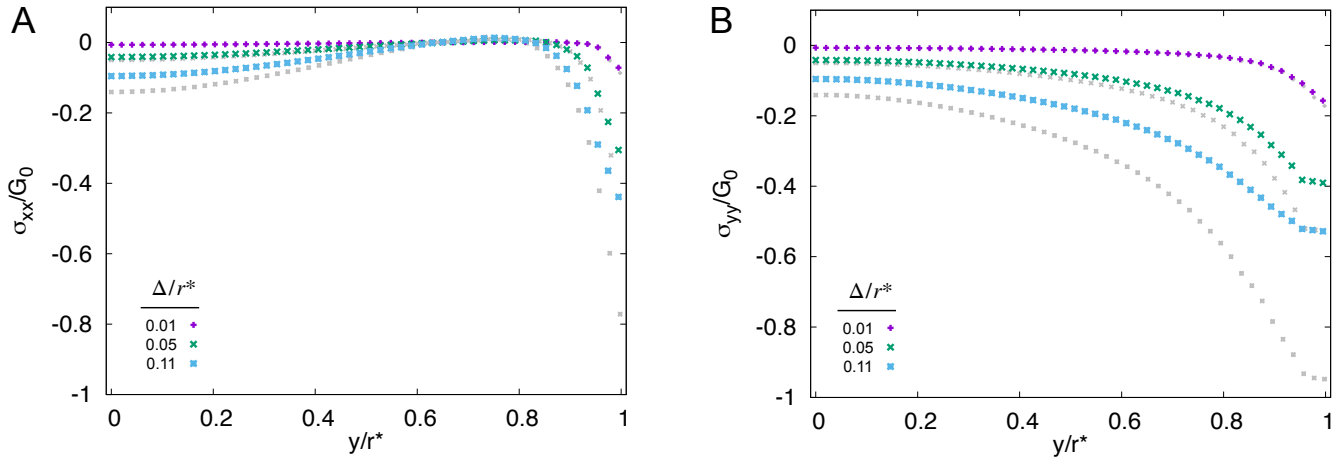

FIG. S12: Comparison between Cauchy stress profiles in simulations with the nonlinear hydrogel model and the St. Venant-Kirchhoff elastic model, plotted against undeformed fully-swollen coordinates (corresponding to an unobstructed equilibrium state for the hydrogel). St. Venant-Kirchhoff results are shown with large colored markers, while hydrogel results are shown in grey. Data corresponding to the same value of Δ/r^* have the same marker shape.

As discussed in the main text, the St. Venant-Kirchhoff model is able to capture the maximum tensile stress reasonably well. However, the compressive stresses in the hydrogel model (and neo-Hookean model, see Fig. S10B) are significantly larger than those in the St. Venant-Kirchhoff model for large deformations.

I. Maximum tensile stresses in weak confinement

In Figs. S9 and S11, the global maximum of principal tensile stress is larger than the theoretical expectation at small indentation depths. These deviations are the result of isolated cells experiencing large tensile stresses on the boundary of the hydrogel where the material loses contact with the obstacle, and we consider it to be an unphysical effect originating with our finite mesh resolution. In Fig. S13, we show how the tension changes as we increase the resolution. At the relatively coarse resolution used for the simulations in this work with 30 vertices along the radius, the anomalous tension appears close to the boundary, while at higher resolutions it is more reliably located on the boundary itself. We compare the maximum principal stress excluding the boundary points (blue crosses in Fig. S13) to the maximum principal stress including the boundary and the maximum tensile stress beneath the obstacle. We find good agreement between the maximum stress excluding the boundary and the theoretical expectation at high resolution. However, since the maximum compression occurs close to the boundary as well, excluding these points systematically creates disagreement between theory and simulation for compressive stresses. Thus, in Fig. 3 we display the maximum and minimum stresses taken along a line connecting the obstacle center to the hydrogel center beneath the top obstacle, as decribed in *Materials and methods*.

J. Symmetry-breaking instability

When obstacles are very close together ($\Delta/r^* > 0.56$ for $r_{\text{obs}}/r^* = 0.3$), simulations show that the hydrogel disk swells primarily along a diagonal, rather than equally in all four pore spaces. This effect is quantified in Fig. S14.

As discussed in the main text, this instability can be understood as the hydrogel prioritizing an elliptical shape over a circular shape. In the weak confinement regime, deformations are relatively localized. Therefore, by symmetry, the hydrogel will swell evenly into all four pores. However, as the confinement increases and the deformation becomes global, maintaining symmetric swelling requires isotropic compression of the center of the hydrogel. Assuming uniform deformations and reasonable elastic parameters, it is less costly for the hydrogel to compress an amount Δ along a single axis, forming an ellipse, than to compress an amount Δ along two axes, forming a smaller circle. For concreteness, we demonstrate this with a compressible neo-Hookean model (Eq. S45). Compressibility results from the migration of solvent molecules, as shown in ESI Sec. F. To transform a circle into a smaller circle, we impose

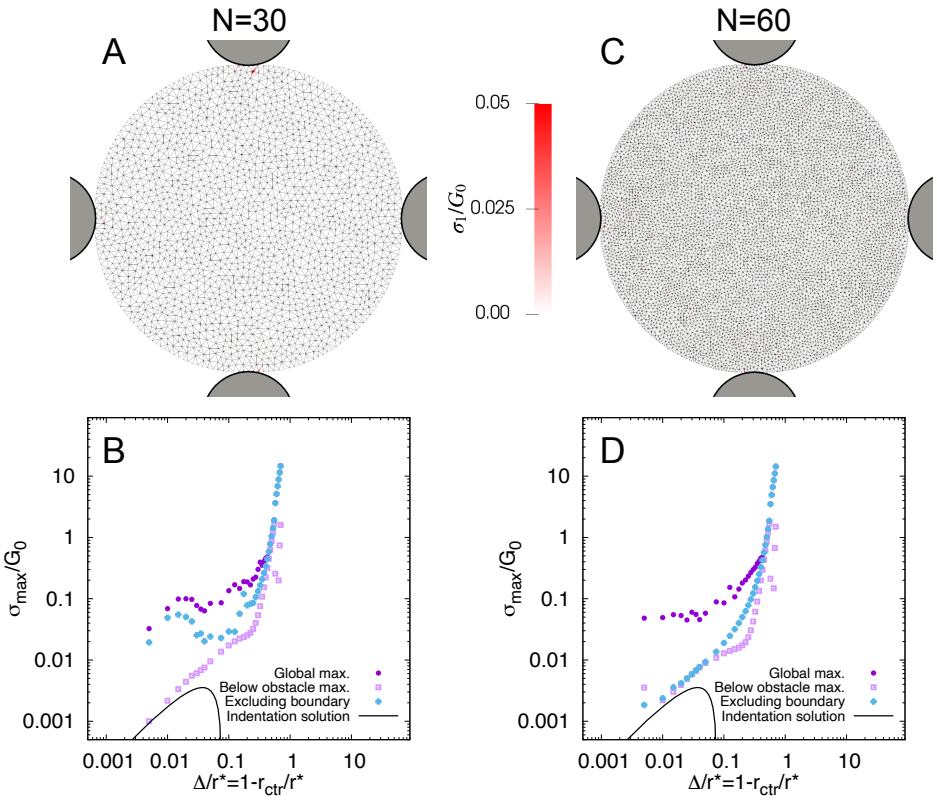

FIG. S13: Large tensile stresses appear at isolated points near where the hydrogel loses contact with an obstacle. (A) Positive values of the principal stresses for $\Delta/r^* = 0.98, r_{obs}/r^* = 0.3$, plotted on top of the deformed hydrogel mesh and rescaled by the fully swollen shear modulus G_0. (B) We compare the maximum principal stresses shown in Fig. 5 of the main text (purple circles) to the maximum principal stress excluding the boundary cells, taken by excluding cells at positions $\geq 95\%$ of the hydrogel radius. Panels (C, D) show the same calculations at twice the resolution.

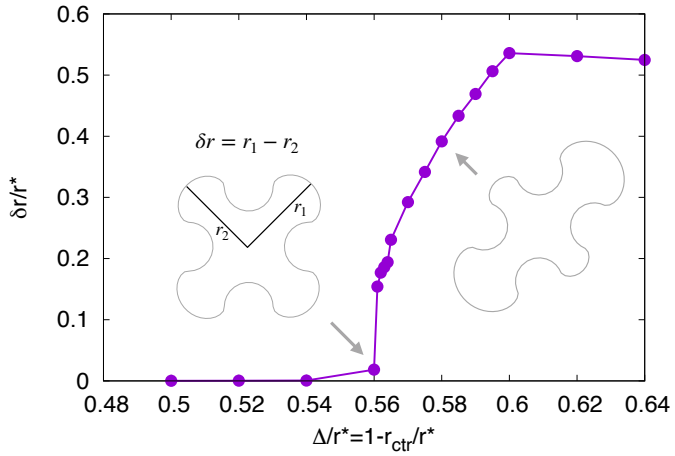

FIG. S14: As Δ/r^* increases (the obstacles are brought closer together), the hydrogel begins to swell preferentially along a diagonal. The difference in the maximum distance from the origin of the top right and top left hydrogel lobe, δr, provides an order parameter for this transition. Insets show the boundary of the hydrogel at the indicated points (obstacles not pictured).

stretches $\lambda_1 = \lambda_2 = 1 - \Delta/r^*$. The energy density is therefore

$$W_{\text{circle}} \propto 2\left(1 - \frac{\Delta}{r^*}\right)^2 - 2 - 2\ln\left[(1-\Delta/r^*)^2\right] + \frac{2\nu}{(1-\nu)}\ln\left[(1-\Delta/r^*)^2\right]^2. \tag{S59}$$

To transform a circle into an ellipse, we impose $\lambda_1 = 1 - \Delta/r^*, \lambda_2 = 1$. The energy for this deformation is

$$W_{\text{ellipse}} \propto \left(1 - \frac{\Delta}{r^*}\right)^2 - 1 - 2\ln\left[1-\Delta/r^*\right] + \frac{2\nu}{(1-\nu)}\ln\left[1-\Delta/r^*\right]^2. \tag{S60}$$

We can expand both expressions in Δ/r^*. At lowest order, both energies are quadratic in Δ/r^*, with the circular deformation having a higher energy than the elliptical deformation as long as $\nu > -1/2$. We can also substitute in the effective Poisson's ratio used in simulations, $\nu = 0.34$ (Eq. 2 of main text), to confirm that the elliptical deformation remains lower in energy as Δ/r^* increases to 1.

[1] Y. Tatara, "On Compression of Rubber Elastic Sphere Over a Large Range of Displacements—Part 1: Theoretical Study," Journal of Engineering Materials and Technology **113**, 285–291 (1991).

[2] Jean-François Louf, Nancy B Lu, Margaret G O'Connell, H Jeremy Cho, and Sujit S Datta, "Under pressure: Hydrogel swelling in a granular medium," Science Advances **7**, eabd2711 (2021).

[3] Adel S Saada, *Elasticity: theory and applications*, Vol. 16 (Elsevier, 2013).

[4] Lev Davidovich Landau, AM Kosevich, Lev Petrovich Pitaevskii, and Evgenii Mikhailovich Lifshitz, *Theory of Elasticity* (Butterworth-Heinemann, Oxford, 1986).

[5] Wei Hong, Xuanhe Zhao, Jinxiong Zhou, and Zhigang Suo, "A theory of coupled diffusion and large deformation in polymeric gels," Journal of the Mechanics and Physics of Solids **56**, 1779–1793 (2008).

[6] Min Kyoo Kang and Rui Huang, "A variational approach and finite element implementation for swelling of polymeric hydrogels under geometric constraints," Journal of Applied Mechanics **77** (2010).

[7] Yue Zheng, Yuhang Hu, and Shengqiang Cai, "Contact mechanics of a gel under constrained swelling," Journal of the Mechanics and Physics of Solids **124**, 427–445 (2019).

[8] Wei Hong, Zishun Liu, and Zhigang Suo, "Inhomogeneous swelling of a gel in equilibrium with a solvent and mechanical load," International Journal of Solids and Structures **46**, 3282–3289 (2009).

[9] Nikolaos Bouklas, Chad M Landis, and Rui Huang, "A nonlinear, transient finite element method for coupled solvent diffusion and large deformation of hydrogels," Journal of the Mechanics and Physics of Solids **79**, 21–43 (2015).

[10] Toyoichi Tanaka, "Kinetics of phase transition in polymer gels," Physica A: Statistical Mechanics and its Applications **140**, 261–268 (1986).

[11] Alessandro Lucantonio, Paola Nardinocchi, and Luciano Teresi, "Transient analysis of swelling-induced large deformations in polymer gels," Journal of the Mechanics and Physics of Solids **61**, 205–218 (2013).

[12] Shawn A Chester and Lallit Anand, "A coupled theory of fluid permeation and large deformations for elastomeric materials," Journal of the Mechanics and Physics of Solids **58**, 1879–1906 (2010).

[13] Michele Curatolo, Paola Nardinocchi, Eric Puntel, and Luciano Teresi, "Transient instabilities in the swelling dynamics of a hydrogel sphere," Journal of Applied Physics **122**, 145109 (2017).

[14] Nikolaos Bouklas and Rui Huang, "Swelling kinetics of polymer gels: comparison of linear and nonlinear theories," Soft Matter **8**, 8194–8203 (2012).

[15] James R Barber, *Elasticity* (Springer, 2002).

[16] James Norman Goodier and Stephen Timoshenko, *Theory of elasticity* (McGraw-Hill, 1970).

[17] Kenneth Langstreth Johnson, *Contact mechanics* (Cambridge University Press, 1987).

[18] DLMF, "*NIST Digital Library of Mathematical Functions*," http://dlmf.nist.gov/, Release 1.1.7 of 2022-10-15, f. W. J. Olver, A. B. Olde Daalhuis, D. W. Lozier, B. I. Schneider, R. F. Boisvert, C. W. Clark, B. R. Miller, B. V. Saunders, H. S. Cohl, and M. A. McClain, eds.

[19] Klaus Bernd Sautter, Manuel Meßmer, Tobias Teschemacher, and Kai-Uwe Bletzinger, "Limitations of the St. Venant–Kirchhoff material model in large strain regimes," International Journal of Non-Linear Mechanics **147**, 104207 (2022).